NANO LETTERS

pubs.acs.org/NanoLett Letter

# Tailoring Valley Polarization of Interlayer Excitons in van der Waals Heterostructure toward Optical Communication

Yi Zhu,† Kong-Liang Zou,† Dong-Xiang Qi,† Jie He, Ruwen Peng,* and Mu Wang*

Cite This: https://doi.org/10.1021/acs.nanolett.5c01583 Read Online

ACCESS | Metrics & More | Article Recommendations | Supporting Information

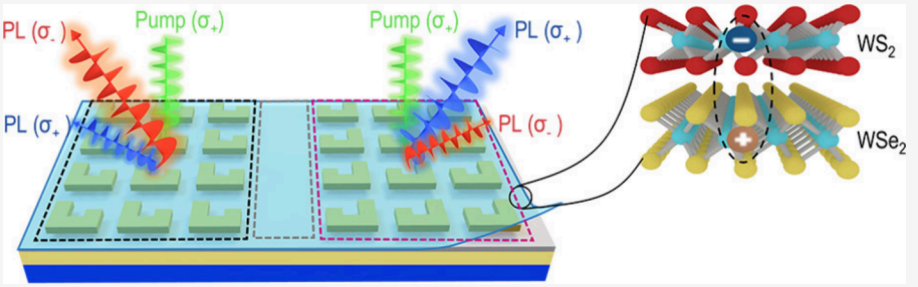


**ABSTRACT:** Controlling the valley polarization of interlayer excitons in van der Waals heterostructures is essential for developing valleytronic devices. Here, we demonstrate the manipulation of valley polarization of interlayer excitons in a monolayer $WSe_2/WS_2$ heterostructure using a dual-handedness metasurface. This metasurface, composed of left- and right-handed gold nanoantenna arrays, exhibits distinct chiral optical responses. Introducing the metasurface into heterostructures significantly enhances the degree of interlayer exciton valley polarization, which quantitatively corresponds to the circular dichroism (CD) of interlayer excitons, via chiral Purcell effects. A negative CD of −16% is yielded via the left-handed metasurface, and a positive CD of +25% is harvested via the right-handed metasurface under $\sigma_+$ excitation of 532 nm at 77 K. Moreover, the CD is tunable with excitation wavelength, reaching a maximum of 38% at 620 nm under $\sigma_-$ excitation, the highest value from interlayer excitons reported so far without applying external fields. Further, we demonstrate that this platform enables direct and byte-invert arithmetic operations for information transmission. This capability highlights its potential for error detection in valleytronics-based optical communication systems.

**KEYWORDS:** *Transition metal dichalcogenides, heterostructures, interlayer excitons, chiral metasurfaces, valley polarization enhancement*



Two-dimensional transition-metal dichalcogenides (TMDs) are promising candidates for valleytronic applications, such as valley-addressable laser,[1] nanophotonic circuit,[2] and valley transistor.[3,4] The broken inversion symmetry and strong spin−orbital interaction in monolayer TMDs lead to two degenerate yet inequivalent valley states, K and K', in their band structures, offering a new degree of freedom to store and process information.[5−7] The electrons in these two valley states can be selectively excited with circularly polarized light, generating an imbalanced carrier population in K or K' valleys. Therefore, the circularly polarized photoluminescence (PL) manifests unequal intensity for two chiral components.[8−10] Circular dichroism (CD)[5,11−13] can be defined as $CD = (I_{co} - I_{cross})/(I_{co} + I_{cross})$, where $I_{co}$ is the intensity of the copolarized light and $I_{cross}$ is the intensity of the cross-polarized light. Previous studies have shown valley-polarized PL from intralayer exciton in monolayer molybdenum disulfide ($MoS_2$),[5,8,9,14] molybdenum diselenide ($MoSe_2$),[15,16] tungsten disulfide ($WS_2$),[17,18] and tungsten diselenide ($WSe_2$).[10,19,20] However, electron−hole exchange interactions lead to rapid valley depolarization of intralayer excitons in monolayer TMDs within picoseconds, which restricts their applications in valleytronic devices.[21−24]

Alternatively, stacking different TMD monolayers to a van der Waals (vdW) heterostructure gives rise to interlayer excitons, where the electron and hole are spatially separated in different layers.[25−27] Unlike intralayer excitons, interlayer excitons exhibit a longer valley lifetime (nanoseconds) due to the small overlap of electron−hole wave functions.[28−31] To date, manipulation of CD in TMDs often requires an externally applied electric field,[10,32,33] magnetic field,[34−38] electrochemical doping,[39] and precise twist-angle engineering,[12,40−42] which are challenging for the broad applications of valleytronic devices. On the other hand, metasurfaces have become a key tool in enhancing the optical properties of two-dimensional

Received: March 11, 2025
Revised: May 2, 2025
Accepted: May 5, 2025

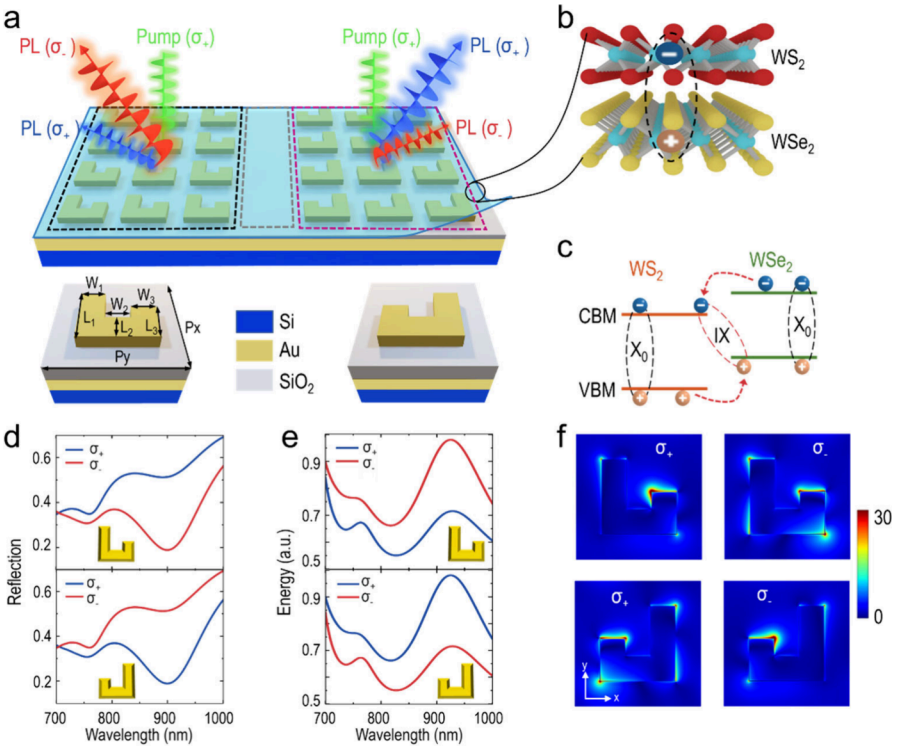


**Figure 1.** (a) Schematic of the monolayer $WSe_2/WS_2$ heterostructure-metasurface structure, where the $WSe_2/WS_2$ heterostructure is placed on the L-MS (black-dashed frame), R-MS (red-dashed frame), and the separating blank region of the metasurface (gray dashed frame), respectively. The unit cells of L-MS (left) and R-MS (right) are shown in the lower row, with the geometrical parameters $L_1$ = 300 nm, $L_2$ = 100 nm, $L_3$ = 170 nm, $W_1$ = $W_2$ = $W_3$ = 100 nm, and $P_x$ = $P_y$ = 500 nm, and the height of the Au nanoantenna is 30 nm. (b) Schematic side view of the $WSe_2/WS_2$ heterostructure. The dashed ellipse depicts the interlayer exciton with holes and electrons in $WSe_2$ and $WS_2$, respectively. (c) Type-II band alignment in monolayer $WSe_2/WS_2$ heterostructure facilitated the formation of interlayer excitons. (d) The simulated reflection spectra of the L-MS and R-MS. (e) The calculated total electromagnetic energy ($U$) of the L-MS and R-MS obtained by integrating the electromagnetic energy in a single unit cell from the nanoantenna top surface down to the gold substrate. (f) The simulated electric field mapping across the unit cell for the L-MS and R-MS with the excitation of $\sigma_+$ and $\sigma_-$ incidence at a resonant wavelength of 905 nm.

materials.[43,44] Recently, chiral metasurfaces with broken mirror symmetry[45,46] have attracted much attention for their pronounced optical activity and CD.[47−50] Leveraging the advantages of chiral metasurfaces, the approach can be applied to tune the valley polarization of intralayer excitons in monolayer TMDs of $MoS_2$,[51−54] $WS_2$,[55] and $WSe_2$.[11,43,56−58] This strategy controls the interaction between the plasmonic resonances of the chiral metasurface and the valley-polarized intralayer exciton to enhance the emission rates in a specific valley. Naturally, combining chiral metasurfaces with van der Waals heterostructures may offer a promising way to modulate the valley polarization of interlayer excitons, which benefit from both the chiral optical responses of metasurfaces and the long lifetime of the interlayer exciton in heterostructures.

In this Letter, we report a dual-handedness metasurface designed to enhance the CD of interlayer excitons in a $WSe_2/WS_2$ heterostructure and show its potential optical communication applications. Our metasurface comprises left- and right-handed sections, separated by a blank region. The CD of interlayer excitons in the blank region is 4% at 77 K. It reaches −16% via the left-handed metasurface and +25% via the right-handed metasurface under an $\sigma_+$ excitation of 532 nm at the same temperature. Helicity-resolved photoluminescence excitation (PLE) spectroscopy reveals an increased CD up to 38% as the wavelength of $\sigma_-$ excitation corresponds to the bandgap of $WS_2$. Here $\sigma_+$ denotes right-handed circular polarization and $\sigma_-$ denotes left-handed circular polarization. Furthermore, we demonstrate the heterostructure-metasurface system as a potential bifunctional device for optical information transmission. We encode the input message "NJU" with Morse code. When the encoded light is focused on the right-handed metasurface, the output message remains "NJU". However, focusing on the left-handed metasurface results in the output message "REED". This experiment confirms the capability of this device for both direct and byte-inverted transmission, which is beneficial for error detection in optical communication.

## DESIGNING A DUAL-HANDEDNESS METASURFACE TO UPHOLD $WSE_2/WS_2$ HETEROSTRUCTURE

A schematic of the designed structure is illustrated in Figure 1a. The dual-handedness metasurface is fabricated on a $SiO_2$-gold bilayer on a silicon substrate. In the $x$−$y$ plane, the metasurface is divided into three regions: the left part of the metasurface (L-MS) is a $\eta$-shaped gold nanoantenna array; the right part of the metasurface (R-MS) contains a mirror-imaged array of the L-MS nanoantenna; and the center part does not have any structure and serves as a separating blank region. To investigate the chiral optical response of the device, we perform finite-difference time-domain (FDTD) simulations. The resonant wavelength is designed at 905 nm (the interlayer exciton PL wavelength) by selecting $L_1$ = 300 nm, $L_2$ = 100 nm, $L_3$ = 170 nm, and $W_1$ = $W_2$ = $W_3$ = 100 nm, with a spatial


https://doi.org/10.1021/acs.nanolett.5c01583
Nano Lett. XXXX, XXX, XXX−XXX

lattice period of 500 nm. The calculated reflection spectra of L-MS and R-MS are shown in Figure 1d. It shows that the resonance of the L-MS and R-MS both occur around 905 nm. We simulate the electric and magnetic fields distribution in the gold nanoantenna-$SiO_2$-gold cavity and calculate the total electromagnetic energy $U$ as the sum of the electric and magnetic energy,[59] $U = \frac{1}{4}\int\left(\frac{d(\omega\epsilon)}{d\omega}|E|^2 + \frac{d(\omega\mu)}{d\omega}|H|^2\right)d^3r$ where $E$ and $H$ are the electric and magnetic fields, and $\epsilon$ and $\mu$ are the permittivity and permeability, respectively. The integration is carried out across a single unit cell, from the top surface of the nanoantenna to the gold substrate, where the dispersive materials are considered. On the L-MS, a high resonance peak in the total electromagnetic energy is observed in $\sigma_-$ excitation, indicating a localized plasmonic resonance mode with strong electromagnetic confinement. This resonance leads to significantly higher energy under $\sigma_-$ excitation than $\sigma_+$ excitation (see the upper panel of Figure 1e). In contrast, on the R-MS, the total energy is more significant in $\sigma_+$ excitation (as shown in the lower panel of Figure 1e). This difference is attributed to the localized plasmonic mode, which confines more electromagnetic energy for $\sigma_+$ excitation. To further investigate the physical mechanism of this energy difference, we simulate the electric field distribution on the surface of the gold nanoantenna at the resonant wavelength (905 nm) in both $\sigma_+$ and $\sigma_-$ excitations. It follows that on the L-MS, the electric field intensity is more vigorous for $\sigma_-$ excitation (upper panel of Figure 1f). In contrast, on the R-MS, the electric field is more substantial for $\sigma_+$ excitation (lower panel of Figure 1f). The enhanced electric field intensity indicates a higher concentration of electromagnetic energy within the cavity, leading to a higher total electromagnetic energy $U$. These results confirm that the $\eta$-shaped or its mirror-imaged gold nanoantenna exhibits strong optical chirality[60,61] at the resonant wavelength due to the broken inversion symmetry, resulting in distinct optical responses to $\sigma_+$ and $\sigma_-$ incidence. Structural asymmetry is crucial in generating different near-field enhancements, leading to distinct chiral optical response.

## CHIRAL PURCELL EFFECTS ENHANCE THE DEGREE OF THE INTERLAYER EXCITON VALLEY POLARIZATION

In each unit cell, the sandwich structure realizes the optical field constraint by vertically reflecting the upper gold nanoantenna and the lower solid gold layer. Moreover, in the horizontal direction, it relies on the localized surface plasmon resonance effect of the top gold nanoantenna to achieve optical field localization. Eventually, it forms a nanocavity system that limits the optical field in three-dimensional space.

To modulate the degree of interlayer exciton valley polarization, which quantitatively corresponds to the CD of interlayer excitons,[13] the monolayer $WSe_2/WS_2$ heterostructure is placed on the dual-handedness metasurface, as illustrated in Figure 1a,b. The heterostructure exhibits type-II band alignment: the electrons of $WSe_2$ hop to the conduction band of $WS_2$, and the holes of $WS_2$ hop to the valence band of $WSe_2$. Meanwhile, the interlayer exciton is naturally produced by the spatially separated electron−hole pairs due to Coulomb interactions, as shown in Figure 1c. Considering that each unit cell of the gold metasurface acts as a chiral nanocavity, the helicity-dependent strong electric fields may induce the chiral Purcell effect[54] in the $WSe_2/WS_2$ heterostructure-metasurface structure.

Now we consider that the valley-polarized emission can be modified by the chiral Purcell effect[54,56,62] in the current $WSe_2/WS_2$ heterostructure-metasurface structure. We first define $\rho^+$ (or $\rho^-$) as the local density of states (LDOS) on the metasurface with $\sigma_+$ (or $\sigma_-$) dipole excitation and $\rho_0$ as the LDOS in the vacuum. We calculate the normalized circularly polarized LDOS,[54,63] i.e., $\rho^+/\rho_0$ (or $\rho^-/\rho_0$). Figure 2a shows

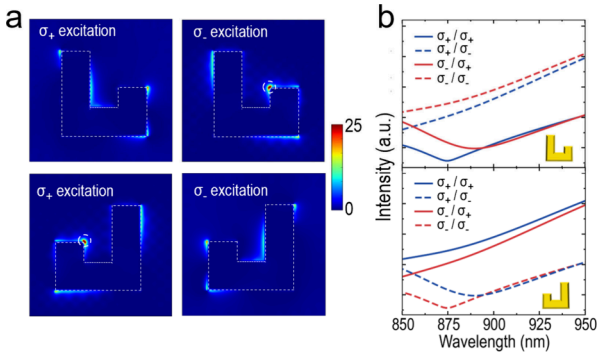


**Figure 2.** (a) LDOS of L-MS and R-MS with $\sigma_+$ and $\sigma_-$ dipole excitation at the resonant wavelength of 905 nm, respectively. (b) The simulated circularly polarized far-field PL spectra out of L-MS and R-MS, respectively. The circularly polarized far field PL is calculated by placing the circularly polarized dipoles at the LDOS maximum spot (marked by the white dashed circle in Figure 2a). Here, $\sigma_+/\sigma_\pm$ stands for the $\sigma_\pm$ resolved far field PL spectra excited by $\sigma_+$ dipoles, and $\sigma_-/\sigma_\pm$ stands for the $\sigma_\pm$ resolved far field PL spectra excited by $\sigma_-$ dipoles.

the simulated LDOS of L-MS and R-MS with both $\sigma_+$ and $\sigma_-$ dipole excitations at a resonant wavelength of 905 nm. It is shown that for L-MS, the LDOS $\rho^-/\rho_0$ reaches the maximum at the corner marked by the white dashed circle under $\sigma_-$ dipoles excitation (to see the upper right panel of Figure 2a). This suggests[63] that the L-MS promotes a higher spontaneous emission rate for $\sigma_-$ dipoles, leading to a higher Purcell factor for $\sigma_-$ dipoles. Further if placing the circularly polarized dipoles at the $\rho^-/\rho_0$ maximum spot on L-MS, the calculated far-field PL spectra out of the L-MS (as shown in the upper panel of Figure 2b) reveal that the emission modified by LDOS always favors stronger $\sigma_-$ light regardless of the incident polarization. Similarly, for R-MS, the LDOS $\rho^+/\rho_0$ reaches the maximum at the corner marked by the dashed circle under $\sigma_+$ dipole excitation (to see the lower left panel of Figure 2a), and the emission out of the R-MS always generates stronger $\sigma_+$ light (as shown in the lower panel of Figure 2b). All these simulations indicate that the valley-polarized emission in this system is significantly modified by the chiral Purcell effects in L-MS and R-MS. More simulations are given in Figure S1 of Supporting Information.

## SAMPLE FABRICATION AND VALLEY POLARIZATION OF INTERLAYER EXCITONS

Experimentally, we first fabricate the sample by depositing a 100 nm-thick gold reflecting layer and a 90 nm-thick $SiO_2$ dielectric layer on a Si substrate by magnetron sputtering. Then, we fabricated the gold unit cell arrays using e-beam lithography to make the left (L-MS) and right (R-MS) parts of the metasurface. The L-MS and R-MS are separated by 5 $\mu$m, where no structures are fabricated. The mechanically exfoliated $WSe_2$ monolayer is transferred to cover three regions of the


https://doi.org/10.1021/acs.nanolett.5c01583
Nano Lett. XXXX, XXX, XXX−XXX

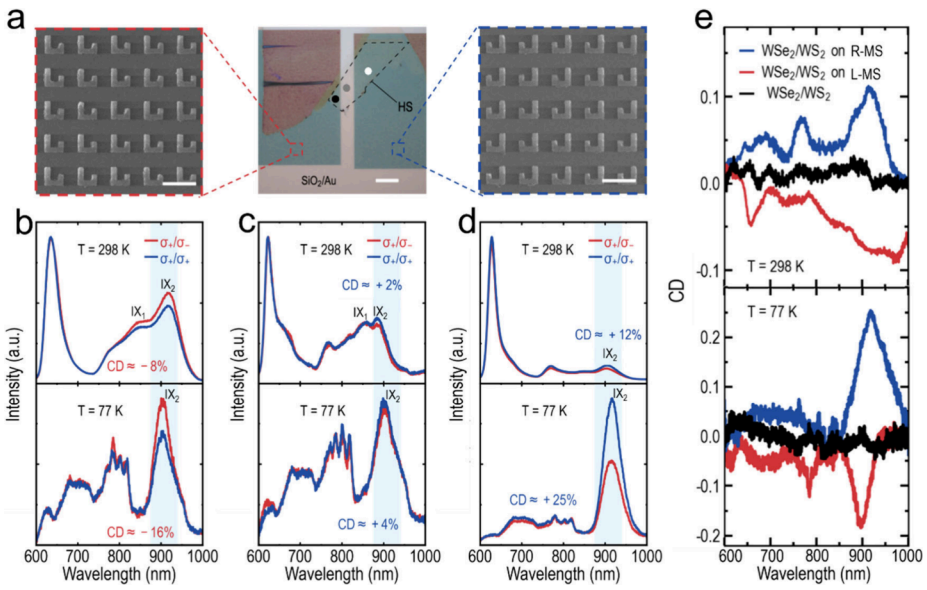


**Figure 3.** (a) The optical microscope image of the $WSe_2/WS_2$ heterostructure-metasurface, where heterostructure flake is in the dashed black area. Here the scale bar is 10 $\mu$m. Left and right show the scanning electron micrographs of metasurfaces, where each scale bar is 500 nm. The measured valley-polarized PL spectra of $WSe_2/WS_2$ heterostructure at both 298 K and 77 K, which covers on: (b) the L-MS, (c) the separating blank region of the metasurface, and (d) the R-MS, respectively. Here, $IX_1$ and $IX_2$ are marked, and $\sigma_+/\sigma_\pm$ stands for the $\sigma_\pm$ resolved PL spectra excited by $\sigma_+$ incidence in (b)-(d). (e) The circular dichroism spectra of the bare $WSe_2/WS_2$ heterostructure (black) and the heterostructure covering the metasurface (red, blue) at 298 K and 77 K, respectively.

metasurface using the dry transfer method. A mechanically exfoliated $WS_2$ monolayer is transferred over the $WSe_2$ monolayer (about 0° twist) using the same method. According to ref 64, the interlayer exciton PL wavelength in a 0° stacked $WS_2/WSe_2$ heterostructure is around 905 nm, which aligns with the resonance wavelength of the chiral structures we designed. Figure 3a shows the optical micrography of the $WSe_2/WS_2$ heterostructure-metasurface. The black, gray, and white dots represent the excitation sites on the three distinct regions marked by the dashed line frames in Figure 1a, respectively. Scanning electron micrographs of the L-MS and R-MS are shown in Figure 3a as well. Circularly polarized PL can determine the valley polarization of the interlayer exciton in the $WSe_2/WS_2$ heterostructure. In the experiments, we utilize $\sigma_+$ ($\sigma_-$) incidence to excite the heterostructure and then analyze both $\sigma_+$ and $\sigma_-$ components of the PL signal. The excitation wavelength is 532 nm, corresponding to an energy ($E_{pump}$ = 2.33 eV) much higher than that of the neutral intralayer excitons in monolayer $WS_2$ ($E_{X_0}$ = 2 eV) and $WSe_2$ ($E_{X_0}$ = 1.66 eV). This configuration ensures the excitation of the interlayer excitons at 905 nm. Figure 3b–d illustrates the valley-polarized PL spectra of the $WSe_2/WS_2$ heterostructure on the L-MS, the separating blank region, and the R-MS, respectively. Here, $\sigma_+/\sigma_\pm$ stands for the $\sigma_\pm$ resolved PL spectra excited by the $\sigma_+$ incidence.

At room temperature, the heterostructure exhibits four PL peaks: neutral intralayer excitons ($X_0$) in monolayer $WS_2$ at 620 nm, neutral intralayer excitons ($X_0$) in monolayer $WSe_2$ at 765 nm, and two interlayer excitons ($IX_1$ and $IX_2$) in the near-infrared region. For the $WSe_2/WS_2$ heterostructure on the separating blank region of the metasurface, the valley-resolved PL spectra indicate that the CD of $IX_2$ is about 2% at ambient temperature (upper panel of Figure 3c). Meanwhile, for the $WSe_2/WS_2$ heterostructure on L-MS, the CD of $IX_2$ exhibits a sign reverse and reaches ∼ −8% (upper panel of Figure 3b). Similarly, for the $WSe_2/WS_2$ heterostructure on R-MS, the CD of $IX_2$ is increased to about 12% (upper panel of Figure 3d).

When the temperature is dropped to 77 K, the $IX_2$ exciton dominates. The CD of the $IX_2$ on the separating blank region of the metasurface is increased to about 4% (lower panel of Figure 3c). More specifically, the CD of $IX_2$ on L-MS and R-MS enhances from ∼ −8% to ∼ −16% and from ∼ +12% to ∼ +25%, respectively (lower panel of Figure 3b,d). Figure 3e compares the CD of $WSe_2/WS_2$ heterostructure on the L-MS, separating blank region, and R-MS at 298 K (upper panel of Figure 3e) and 77 K (lower panel of Figure 3e), respectively. Therefore, by covering the $WSe_2/WS_2$ heterostructure on R-MS, the CD of $IX_2$ is enhanced, while on L-MS, the CD is inverted in sign and the value is enhanced as well. These results confirm that we are able to manipulate the valley polarization of interlayer excitons in the $WSe_2/WS_2$ heterostructure at 298 and 77 K. The PL spectra excited by $\sigma_-$ light are shown in Supporting Information in Figure S2.

To investigate the effect of excitation wavelength on the CD of $IX_2$, we utilize helicity-resolved photoluminescence excitation (PLE) spectroscopy to measure the dependence of interlayer exciton PL intensity on the excitation wavelength under $\sigma_+$ and $\sigma_-$ excitation, respectively. The $WSe_2/WS_2$ heterostructure on the L-MS is excited with $\sigma_-$ light possessing an excitation wavelength ranging from 510 to 620 nm. The detected $\sigma_-$ and $\sigma_+$ components of the PL signal near the $IX_2$ wavelength (from 875 to 940 nm) at 77 K are shown in Figure 4a. It can be observed that the PL intensity increases as the excitation wavelength approaches 620 nm (approximately corresponding to the bandgap of $WS_2$). This enhancement is attributed to the increased absorption near the excitation wavelength and hence the increased exciton formation rate, thus resulting in an amplified PL signal. Actually when the excitation wavelength approaches 620 nm, the photon energy matches the direct bandgap of monolayer $WS_2$, leading to electronic transitions primarily from the valence band


https://doi.org/10.1021/acs.nanolett.5c01583
Nano Lett. XXXX, XXX, XXX−XXX

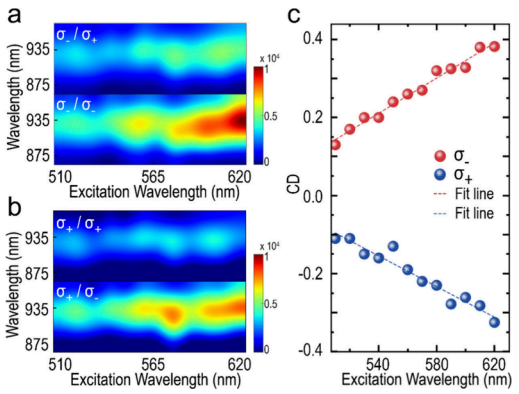


**Figure 4.** The interlayer exciton PLE spectra at 77 K in the $WSe_2$/$WS_2$ heterostructure on the L-MS. The measured valley-polarized interlayer exciton PL spectra plotted as a function of excitation wavelength with (a) $\sigma_-$ excitation and (b) $\sigma_+$ excitation. Here, $\sigma_-/\sigma_\pm$ stands for the $\sigma_\pm$ resolved PL spectra excited by $\sigma_-$ incidence, and $\sigma_+/\sigma_\pm$ stands for the $\sigma_\pm$ resolved PL spectra excited by $\sigma_+$ incidence. (c) The CD value measured at 910 nm as the excitation wavelength was varied from 510 to 620 nm. The blue and red dots represent the CD value with $\sigma_+$ excitation and $\sigma_-$ excitation, respectively. The blue and red dashed lines are fits for the $\sigma_+$ and $\sigma_-$ excitations, respectively.

maximum to the conduction band minimum. It has been reported that the band-edge excitation can reduce the phonon-assisted intervalley scattering in the conduction band, which in turn enhances the circular dichroism response.[65,66] A similar result with the excitation of $\sigma_+$ incident light is also observed, as shown in Figure 4b. Notably, the $\sigma_-$ component of the detected PL intensity is always higher than the $\sigma_+$ component due to L-MS enhancing the spontaneous emission of the $\sigma_-$ exciton.

Figure 4c shows that the CD of the interlayer exciton enhances as the excitation wavelength gradually approaches the one corresponding to the bandgap of $WS_2$ (620 nm) in the $WSe_2$/$WS_2$ heterostructure on the L-MS. With the excitation of 510 nm incidence, the interlayer exciton shows a CD of 13% with $\sigma_-$ excitation. When the excitation wavelength is increased to 620 nm, the CD jumps significantly to 38% with $\sigma_-$ excitation. The CD value might be further enhanced by introducing a metasurface based on chiral quasi-bound states in the continuum,[67] lowering the temperature or introducing the Zeeman-splitting effect by applying a magnetic field.[57]

## POTENTIAL OPTICAL COMMUNICATION WITH VALLEY POLARIZATION

Error detection in optical communication systems is crucial for ensuring data integrity, especially in high-speed and quantum communication. It can be achieved through techniques such as one's complement.[68] This method detects errors caused by bit flips in the data transmission. The sender transmits both the data and its one's complement, which is obtained by flipping each bit of the original data. Upon receiving the data and its complement, the receiver recalculates the one's complement based on the received data and compares it with the received one's complement. If the two are identical, the data are considered without error in transmission. This strategy ensures that both overflows and simple bit errors are more likely to be caught. Considering that the valley polarization of the interlayer exciton PL can be controlled, we design an optical communication approach that allows both direct and byte-invert transmission. Figure 5a shows the experimental setup, where the 532 nm laser passes through a linear polarizer and a quarter-wave plate (QWP). The input message "NJU" is encoded with Morse code.[69,70] The Morse code represents letters and numbers using sequences of dots (short signals) and dashes (long signals), and the timing of these signals is crucial for the correct interpretation. According to standard Morse timing rules, a dot (·) represents '1', a dash (—) represents '111', an intracharacter gap is a short pause between the dots and dashes within a single character and is represented

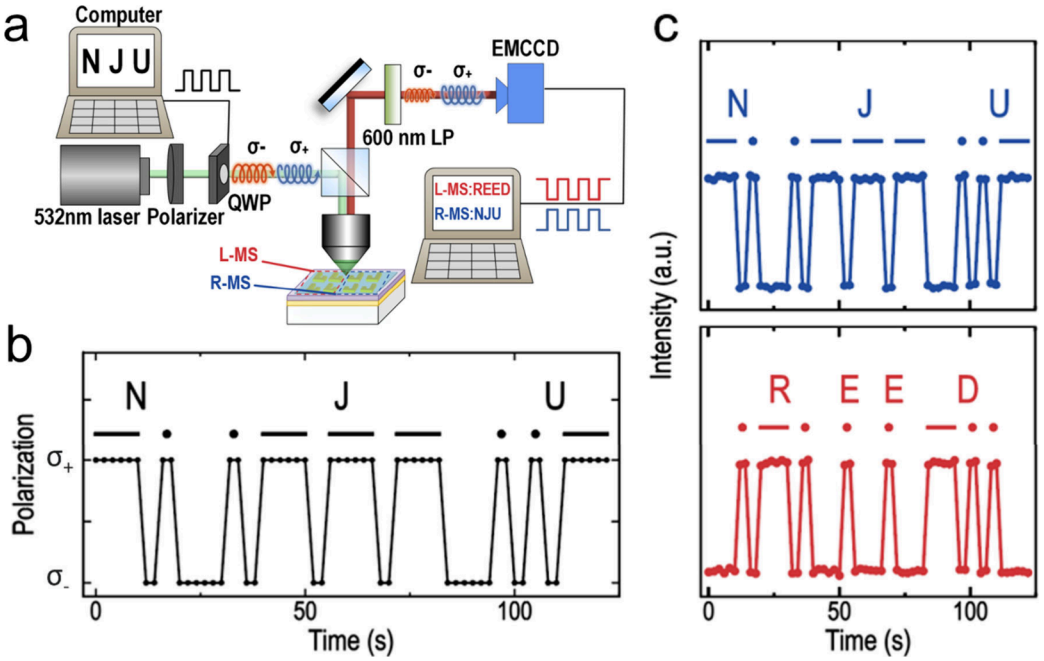


**Figure 5.** (a) Schematic diagram of the communication system. (b) The input signals. (c) Waveforms of output light signals emitted by the heterostructure on the R-MS (upper panel) and L-MS (lower panel).


https://doi.org/10.1021/acs.nanolett.5c01583
Nano Lett. XXXX, XXX, XXX−XXX

by '0', and a short gap between letters is represented by '000'. Using this encoding scheme, each character in 'NJU' is separately encoded as follows: 'N' is encoded as '11101', 'J' is encoded as '1011101110111', 'U' is encoded as '1010111'. When these encoded characters are concatenated with the separator '000' in between, the complete message 'NJU' is encoded as '1110100010111011101110001010111', as shown in Figure 5b. This encoded sequence is then transmitted to the controller, which controls the rotation of QWP. When the controller receives a "1", the fast axis of the QWP will be rotated to −45° with respect to the horizontal direction; when the controller gets a "0", the fast axis of the QWP will be rotated to +45° with respect to the horizontal direction. Therefore, when the controller receives a "1", the emitted light is $\sigma_+$; when it receives a "0", the emitted light is $\sigma_-$.

When the modulated incidence is focused at R-MS, the PL intensity excited by $\sigma_+$ is higher. Therefore, the time series of PL intensity collected by the electron-multiplying charge-coupled device (EMCCD) corresponds to '1110100010111011101110001010111', which can be decoded as "NJU", as shown in the upper panel of Figure 5c. However, if the modulated light is focused at L-MS, the PL intensity excited by $\sigma_-$ is higher. Hence, the PL intensity time series collected by the EMCCD at L-MS is '000101110100010001000111010100O' instead, which is decoded as 'REED', as shown in the lower panel of Figure 5c. In this way, the $WSe_2/WS_2$ heterostructure-metasurface acts as a bifunctional device for transmitting optical messages and achieves both direct and byte-invert transmission in optical communication. In principle, we can sum each byte of the direct and byte-inverted transmission outputs, respectively. If every resulting byte equals 1 after this operation, then the data transmission is accurate. Otherwise, errors occurred in transmission. Therefore, the byte-inverted transmission helps to maintain data integrity by reducing the likelihood of errors. This can be particularly useful in optical communication systems, when signal degradation may occur over long distances.

In conclusion, we tuned the valley polarization of the interlayer exciton by covering the $WSe_2/WS_2$ heterostructure on a dual-handedness metasurface. Physically, each unit cell of the metasurface acts as a chiral nanocavity, and the helicity-dependent strong electric fields induce chiral Purcell effects, which eventually modify the valley-polarized emission of interlayer excitons. With $\sigma_+$ excitation, the interlayer exciton CD in $WSe_2/WS_2$ heterostructures is significantly enhanced on a right-handed metasurface, while on a left-handed metasurface it is sign-inverted with an increased absolute value. Furthermore, the CD of interlayer excitons increases up to 38% as the $\sigma_-$ excitation wavelength corresponds to the bandgap of $WS_2$. Moreover, the $WSe_2/WS_2$ heterostructure-metasurface can serve as a bifunctional device for transmitting optical messages and achieving both direct and byte-invert transmission. This functionality enhances data stability and improves error detection, ensuring high integrity in communication systems.

## METHODS

**Simulation.** All simulations are carried out using the finite-difference time-domain (FDTD) method. In the simulation, periodic boundary conditions in the *x*- and *y*-directions and perfectly matched layer (PML) boundary conditions in the *z*-direction are applied. Plane-wave sources with wavelengths in the range of 700−1000 nm are placed 1 $\mu$m from the structure.

**Sample Preparation.** Au reflection layer (100 nm) and $SiO_2$ dielectric layer (90 nm) are deposited on the polished Si substrate using a magnetron sputtering system. A layer of photoresist is spin-coated onto the $SiO_2$ dielectric layer. Then, electron beam lithography (EBL) is employed to define the designed pattern on the sample. After development, a chiral pattern is formed on the photoresist layer. A 30 nm-thick Au layer is then deposited on the sample by electron beam evaporation. Then we apply the chemical lift-off technique by soaking the sample in a resist remover to peel off the photoresist layer. In this way, only the desired Au patterns survive on the $SiO_2$ layer. Monolayer $WSe_2$ and $WS_2$ flakes are mechanically exfoliated and transferred onto the chiral metasurface in a sequential manner to form a heterostructure. Both monolayers are identified by optical microscopy and confirmed by PL and Raman spectra, as shown in Supporting Information in Figure S3.

**Optical Measurements.** Low-temperature PL measurements are conducted in a temperature-controlled liquid nitrogen bath cryostat (sample in vacuum). PL spectra are acquired on a confocal micro-Raman system (Princeton Instruments, Trenton, NJ) with a 100× objective lens. The excitation laser is a 532 nm CW laser focusing on a diffraction-limited spot of about 1 $\mu$m. A broadband linear polarizer and a quarter-wave plate (532 nm) are used to initiate circularly polarized light. A pair of broadband linear polarizers and a quarter-wave plate (690−1200 nm) are used as the analyzer placed before the spectrometer.

## ASSOCIATED CONTENT

### Supporting Information

The Supporting Information is available free of charge at https://pubs.acs.org/doi/10.1021/acs.nanolett.5c01583.

Simulated PL spectra, valley-polarized PL spectra, Raman and PL spectra (PDF)

## AUTHOR INFORMATION


### Corresponding Authors

**Ruwen Peng** − *National Laboratory of Solid State Microstructures, School of Physics, Collaborative Innovation Center of Advanced Microstructures, and Jiangsu Physical Science Research Center, Nanjing University, Nanjing 210093, China;* orcid.org/0000-0003-0424-2771; Email: rwpeng@nju.edu.cn

**Mu Wang** − *National Laboratory of Solid State Microstructures, School of Physics, Collaborative Innovation Center of Advanced Microstructures, and Jiangsu Physical Science Research Center, Nanjing University, Nanjing 210093, China;* orcid.org/0000-0002-3823-1272; Email: muwang@nju.edu.cn

### Authors

**Yi Zhu** − *National Laboratory of Solid State Microstructures, School of Physics, Collaborative Innovation Center of Advanced Microstructures, and Jiangsu Physical Science Research Center, Nanjing University, Nanjing 210093, China*

**Kong-Liang Zou** − *National Laboratory of Solid State Microstructures, School of Physics, Collaborative Innovation Center of Advanced Microstructures, and Jiangsu Physical*




https://doi.org/10.1021/acs.nanolett.5c01583
Nano Lett. XXXX, XXX, XXX−XXX

*Science Research Center, Nanjing University, Nanjing 210093, China*

**Dong-Xiang Qi** − *National Laboratory of Solid State Microstructures, School of Physics, Collaborative Innovation Center of Advanced Microstructures, and Jiangsu Physical Science Research Center, Nanjing University, Nanjing 210093, China*

**Jie He** − *National Laboratory of Solid State Microstructures, School of Physics, Collaborative Innovation Center of Advanced Microstructures, and Jiangsu Physical Science Research Center, Nanjing University, Nanjing 210093, China*

Complete contact information is available at: https://pubs.acs.org/10.1021/acs.nanolett.5c01583

### Author Contributions

†(Y.Z., K.-L.Z., D.-X.Q.) These authors contributed equally to this work. R.P.,Y.Z., and M.W. conceived this work. Y.Z. fabricated the device with the assistance of J.H.; Y.Z., K.L.Z., and D.X.Q. performed the optical experiments; R.P. and M.W. directed and supervised the research. Y.Z., D.X.Q., R.P., and M.W. wrote the manuscript.

### Notes

The authors declare no competing financial interest.

## ■ ACKNOWLEDGMENTS

The work was supported by the National Key R&D Program of China (Grant Nos. 2022YFA1404303 and 2020YFA0211300), the National Natural Science Foundation of China Grant No. 12234010), and the Natural Science Foundation of Jiangsu Province (No. BK20233001).

## ■ REFERENCES

(1) Duan, X.; Wang, B.; Rong, K.; Liu, C. L.; Gorovoy, V.; Mukherjee, S.; Kleiner, V.; Koren, E.; Hasman, E. Valley-addressable monolayer lasing through spin-controlled Berry phase photonic cavities. *Science* **2023**, *381* (6665), 1429−1432.

(2) Chen, Y.; Qian, S.; Wang, K.; Xing, X.; Wee, A.; Loh, K. P.; Wang, B.; Wu, D.; Chu, J.; Alu, A.; Lu, P.; Qiu, C. W. Chirality-dependent unidirectional routing of $WS_2$ valley photons in a nanocircuit. *Nat. Nanotechnol* **2022**, *17*, 1178.

(3) Li, L.; Shao, L.; Liu, X.; Gao, A.; Wang, H.; Zheng, B.; Hou, G.; Shehzad, K.; Yu, L.; Miao, F.; Shi, Y.; Xu, Y.; Wang, X. Room-temperature valleytronic transistor. *Nat. Nanotechnol* **2020**, *15* (9), 743−749.

(4) Mak, K. F.; McGill, K. L.; Park, J.; McEuen, P. L. Valleytronics. The valley Hall effect in $MoS_2$ transistors. *Science* **2014**, *344* (6191), 1489−1492.

(5) Cao, T.; Wang, G.; Han, W.; Ye, H.; Zhu, C.; Shi, J.; Niu, Q.; Tan, P.; Wang, E.; Liu, B.; Feng, J. Valley-selective circular dichroism of monolayer molybdenum disulphide. *Nat. Commun.* **2012**, *3*, 887.

(6) Xiao, D.; Liu, G. B.; Feng, W.; Xu, X.; Yao, W. Coupled spin and valley physics in monolayers of $MoS_2$ and other group-VI dichalcogenides. *Phys. Rev. Lett.* **2012**, *108* (19), 196802.

(7) Xu, X.; Yao, W.; Xiao, D.; Heinz, T. F. Spin and pseudospins in layered transition metal dichalcogenides. *Nat. Phys.* **2014**, *10* (5), 343−350.

(8) Mak, K. F.; He, K.; Shan, J.; Heinz, T. F. Control of valley polarization in monolayer $MoS_2$ by optical helicity. *Nat. Nanotechnol* **2012**, *7* (8), 494−498.

(9) Zeng, H.; Dai, J.; Yao, W.; Xiao, D.; Cui, X. Valley polarization in $MoS_2$ monolayers by optical pumping. *Nat. Nanotechnol* **2012**, *7* (8), 490−493.

(10) Jones, A. M.; Yu, H.; Ghimire, N. J.; Wu, S.; Aivazian, G.; Ross, J. S.; Zhao, B.; Yan, J.; Mandrus, D. G.; Xiao, D.; Yao, W.; Xu, X. Optical generation of excitonic valley coherence in monolayer $WSe_2$. *Nat. Nanotechnol* **2013**, *8* (9), 634−638.

(11) Lin, H. T.; Chang, C. Y.; Cheng, P. J.; Li, M. Y.; Cheng, C. C.; Chang, S. W.; Li, L. L. J.; Chu, C. W.; Wei, P. K.; Shih, M. H. Circular Dichroism Control of Tungsten Diselenide ($WSe_2$) Atomic Layers with Plasmonic Metamolecules. *ACS Appl. Mater. Interfaces* **2018**, *10* (18), 15996−16004.

(12) Scuri, G.; Andersen, T. I.; Zhou, Y.; Wild, D. S.; Sung, J.; Gelly, R. J.; Berube, D.; Heo, H.; Shao, L.; Joe, A. Y.; Mier Valdivia, A. M.; Taniguchi, T.; Watanabe, K.; Loncar, M.; Kim, P.; Lukin, M. D.; Park, H. Electrically Tunable Valley Dynamics in Twisted $WSe_2/WSe_2$ Bilayers. *Phys. Rev. Lett.* **2020**, *124* (21), 217403.

(13) Kim, J.; Jin, C.; Chen, B.; Cai, H.; Zhao, T.; Lee, P.; Kahn, S.; Watanabe, K.; Taniguchi, T.; Tongay, S.; Crommie, M. F.; Wang, F. Observation of ultralong valley lifetime in $WSe_2/MoS_2$ heterostructures. *Sci. Adv.* **2017**, *3* (7), No. e1700518.

(14) Shi, W. B.; He, J.; Li, Q. X.; She, X. C.; Wang, D.; Jing, H.; Zhang, R. L.; Zhao, J. Z.; Peng, R. W.; Xu, H.; Wang, M. Asymmetric valley polarization and photoluminescence in $MoS_2/MoO_3$ heterostructure. *Opt. Express* **2019**, *27* (26), 38451−38462.

(15) Kumar, N.; He, J.; He, D.; Wang, Y.; Zhao, H. Valley and spin dynamics in $MoSe_2$ two-dimensional crystals. *Nanoscale* **2014**, *6* (21), 12690−12695.

(16) Wang, G.; Palleau, E.; Amand, T.; Tongay, S.; Marie, X.; Urbaszek, B. Polarization and time-resolved photoluminescence spectroscopy of excitons in $MoSe_2$ monolayers. *Appl. Phys. Lett.* **2015**, *106* (11), 112101.

(17) Nayak, P. K.; Lin, F. C.; Yeh, C. H.; Huang, J. S.; Chiu, P. W. Robust room temperature valley polarization in monolayer and bilayer WS2. *Nanoscale* **2016**, *8* (11), 6035−6042.

(18) Lin, W. H.; Tseng, W. S.; Went, C. M.; Teague, M. L.; Rossman, G. R.; Atwater, H. A.; Yeh, N. C. Nearly 90% Circularly Polarized Emission in Monolayer WS(2) Single Crystals by Chemical Vapor Deposition. *ACS Nano* **2020**, *14* (2), 1350−1359.

(19) Hsu, W. T.; Chen, Y. L.; Chen, C. H.; Liu, P. S.; Hou, T. H.; Li, L. J.; Chang, W. H. Optically initialized robust valley-polarized holes in monolayer $WSe_2$. *Nat. Commun.* **2015**, *6*, 8963.

(20) You, Y.; Zhang, X.-X.; Berkelbach, T. C.; Hybertsen, M. S.; Reichman, D. R.; Heinz, T. F. Observation of biexcitons in monolayer $WSe_2$. *Nat. Phys.* **2015**, *11* (6), 477−481.

(21) Yu, T.; Wu, M. W. Valley depolarization due to intervalley and intravalley electron-hole exchange interactions in monolayer $MoS_2$. *Phys. Rev. B* **2014**, *89* (20), 205303.

(22) Glazov, M. M.; Amand, T.; Marie, X.; Lagarde, D.; Bouet, L.; Urbaszek, B. Exciton fine structure and spin decoherence in monolayers of transition metal dichalcogenides. *Phys. Rev. B* **2014**, *89* (20), 201302.

(23) Lagarde, D.; Bouet, L.; Marie, X.; Zhu, C. R.; Liu, B. L.; Amand, T.; Tan, P. H.; Urbaszek, B. Carrier and polarization dynamics in monolayer $MoS_2$. *Phys. Rev. Lett.* **2014**, *112* (4), No. 047401.

(24) Zhu, C. R.; Zhang, K.; Glazov, M.; Urbaszek, B.; Amand, T.; Ji, Z. W.; Liu, B. L.; Marie, X. Exciton valley dynamics probed by Kerr rotation in$WSe_2$ monolayers. *Phys. Rev. B* **2014**, *90* (16), 161302.

(25) Chiu, M. H.; Li, M. Y.; Zhang, W.; Hsu, W. T.; Chang, W. H.; Terrones, M.; Terrones, H.; Li, L. J. Spectroscopic signatures for interlayer coupling in $MoS_2$-$WSe_2$ van der Waals stacking. *ACS Nano* **2014**, *8* (9), 9649−9656.

(26) Fang, H.; Battaglia, C.; Carraro, C.; Nemsak, S.; Ozdol, B.; Kang, J. S.; Bechtel, H. A.; Desai, S. B.; Kronast, F.; Unal, A. A.; Conti, G.; Conlon, C.; Palsson, G. K.; Martin, M. C.; Minor, A. M.; Fadley, C. S.; Yablonovitch, E.; Maboudian, R.; Javey, A. Strong interlayer coupling in van der Waals heterostructures built from single-layer chalcogenides. *Proc. Natl. Acad. Sci. U. S. A.* **2014**, *111* (17), 6198−6202.

(27) Rivera, P.; Schaibley, J. R.; Jones, A. M.; Ross, J. S.; Wu, S.; Aivazian, G.; Klement, P.; Seyler, K.; Clark, G.; Ghimire, N. J.; Yan, J.; Mandrus, D. G.; Yao, W.; Xu, X. Observation of long-lived interlayer

excitons in monolayer $MoSe_2$-$WSe_2$ heterostructures. *Nat. Commun.* **2015**, *6*, 6242.
(28) Baranowski, M.; Surrente, A.; Klopotowski, L.; Urban, J. M.; Zhang, N.; Maude, D. K.; Wiwatowski, K.; Mackowski, S.; Kung, Y. C.; Dumcenco, D.; Kis, A.; Plochocka, P. Probing the Interlayer Exciton Physics in a $MoS_2$/$MoSe_2$/$MoS_2$ van der Waals Heterostructure. *Nano Lett.* **2017**, *17* (10), 6360−6365.
(29) Miller, B.; Steinhoff, A.; Pano, B.; Klein, J.; Jahnke, F.; Holleitner, A.; Wurstbauer, U. Long-Lived Direct and Indirect Interlayer Excitons in van der Waals Heterostructures. *Nano Lett.* **2017**, *17* (9), 5229−5237.
(30) Nagler, P.; Ballottin, M. V.; Mitioglu, A. A.; Mooshammer, F.; Paradiso, N.; Strunk, C.; Huber, R.; Chernikov, A.; Christianen, P. C. M.; Schuller, C.; Korn, T. Giant magnetic splitting inducing near-unity valley polarization in van der Waals heterostructures. *Nat. Commun.* **2017**, *8* (1), 1551.
(31) Kiemle, J.; Sigger, F.; Lorke, M.; Miller, B.; Watanabe, K.; Taniguchi, T.; Holleitner, A.; Wurstbauer, U. Control of the orbital character of indirect excitons in $MoS_2$/$WS_2$ heterobilayers. *Phys. Rev. B* **2020**, *101* (12), 121404.
(32) Rivera, P.; Seyler, K. L.; Yu, H.; Schaibley, J. R.; Yan, J.; Mandrus, D. G.; Yao, W.; Xu, X. Valley-polarized exciton dynamics in a 2D semiconductor heterostructure. *Science* **2016**, *351* (6274), 688−691.
(33) Wu, S.; Ross, J. S.; Liu, G.-B.; Aivazian, G.; Jones, A.; Fei, Z.; Zhu, W.; Xiao, D.; Yao, W.; Cobden, D.; Xu, X. Electrical tuning of valley magnetic moment through symmetry control in bilayer $MoS_2$. *Nat. Phys.* **2013**, *9* (3), 149−153.
(34) Jiang, C.; Xu, W.; Rasmita, A.; Huang, Z.; Li, K.; Xiong, Q.; Gao, W. B. Microsecond dark-exciton valley polarization memory in two-dimensional heterostructures. *Nat. Commun.* **2018**, *9* (1), 753.
(35) Aivazian, G.; Gong, Z.; Jones, A. M.; Chu, R.-L.; Yan, J.; Mandrus, D. G.; Zhang, C.; Cobden, D.; Yao, W.; Xu, X. Magnetic control of valley pseudospin in monolayer $WSe_2$. *Nat. Phys.* **2015**, *11* (2), 148−152.
(36) Li, Y.; Ludwig, J.; Low, T.; Chernikov, A.; Cui, X.; Arefe, G.; Kim, Y. D.; van der Zande, A. M.; Rigosi, A.; Hill, H. M.; Kim, S. H.; Hone, J.; Li, Z.; Smirnov, D.; Heinz, T. F. Valley splitting and polarization by the Zeeman effect in monolayer $MoSe_2$. *Phys. Rev. Lett.* **2014**, *113* (26), 266804.
(37) Ye, Y.; Xiao, J.; Wang, H.; Ye, Z.; Zhu, H.; Zhao, M.; Wang, Y.; Zhao, J.; Yin, X.; Zhang, X. Electrical generation and control of the valley carriers in a monolayer transition metal dichalcogenide. *Nat. Nanotechnol* **2016**, *11* (7), 598−602.
(38) Wu, W.; Liu, M.; Zhou, J.; Li, J.; Zhang, Y.; Xu, F.; Li, X.; Wu, Y.; Wu, Z.; Kang, J. Chirality-Dependent Valley Polarization in Magnetic van der Waals Heterostructures via Spin-Selective Charge Transfer. *Nano Lett.* **2024**, *24* (21), 6225−6232.
(39) Ye, T.; Li, Y.; Li, J.; Shen, H.; Ren, J.; Ning, C. Z.; Li, D. Nonvolatile electrical switching of optical and valleytronic properties of interlayer excitons. *Light Sci. Appl.* **2022**, *11* (1), 23.
(40) Seyler, K. L.; Rivera, P.; Yu, H.; Wilson, N. P.; Ray, E. L.; Mandrus, D. G.; Yan, J.; Yao, W.; Xu, X. Signatures of moire-trapped valley excitons in $MoSe_2$/$WSe_2$ heterobilayers. *Nature* **2019**, *567* (7746), 66−70.
(41) Tran, K.; Moody, G.; Wu, F.; Lu, X.; Choi, J.; Kim, K.; Rai, A.; Sanchez, D. A.; Quan, J.; Singh, A.; Embley, J.; Zepeda, A.; Campbell, M.; Autry, T.; Taniguchi, T.; Watanabe, K.; Lu, N.; Banerjee, S. K.; Silverman, K. L.; Kim, S.; Tutuc, E.; Yang, L.; MacDonald, A. H.; Li, X. Evidence for moire excitons in van der Waals heterostructures. *Nature* **2019**, *567* (7746), 71−75.
(42) Lian, Z.; Meng, Y.; Ma, L.; Maity, I.; Yan, L.; Wu, Q.; Huang, X.; Chen, D.; Chen, X.; Chen, X.; Blei, M.; Taniguchi, T.; Watanabe, K.; Tongay, S.; Lischner, J.; Cui, Y.-T.; Shi, S.-F. Valley-polarized excitonic Mott insulator in $WS_2$/$WSe_2$ moiré superlattice. *Nat. Phys.* **2024**, *20* (1), 34−39.
(43) Jeong, M.; Ko, B.; Jung, C.; Kim, J.; Jang, J.; Mun, J.; Lee, J.; Yun, S.; Kim, S.; Rho, J. Printable Light-Emitting Metasurfaces with Enhanced Directional Photoluminescence. *Nano Lett.* **2024**, *24* (19), 5783−5790.
(44) Lee, J.; Jeong, M.; Jang, J.; Kim, J.; Mun, J.; Gong, X.; Fang, R.; Yang, Y.; Chae, S. H.; Kim, S.; Rho, J. Bound-States-in-the-Continuum-Induced Directional Photoluminescence with Polarization Singularity in $WS_2$ Monolayers. *Nano Lett.* **2025**, *25* (2), 861−867.
(45) Huang, C.; Feng, Y.; Zhao, J.; Wang, Z.; Jiang, T. Asymmetric electromagnetic wave transmission of linear polarization via polarization conversion through chiral metamaterial structures. *Phys. Rev. B* **2012**, *85* (19), 195131.
(46) Maoz, B. M.; Ben Moshe, A.; Vestler, D.; Bar-Elli, O.; Markovich, G. Chiroptical effects in planar achiral plasmonic oriented nanohole arrays. *Nano Lett.* **2012**, *12* (5), 2357−2361.
(47) Li, Z.; Alici, K. B.; Colak, E.; Ozbay, E. Complementary chiral metamaterials with giant optical activity and negative refractive index. *Appl. Phys. Lett.* **2011**, *98* (16), 161907.
(48) Li, C. Y.; Chen, C.; Liu, Y.; Su, J.; Qi, D. X.; He, J.; Fan, R. H.; Cai, Q.; Li, Q.; Peng, R.; Huang, X. R.; Wang, M. Multiple-polarization-sensitive photodetector based on a perovskite metasurface. *Opt. Lett.* **2022**, *47* (3), 565−568.
(49) Kim, J.; Rana, A. S.; Kim, Y.; Kim, I.; Badloe, T.; Zubair, M.; Mehmood, M. Q.; Rho, J. Chiroptical Metasurfaces: Principles, Classification, and Applications. *Sensors (Basel)* **2021**, *21* (13), 4381.
(50) Jang, J.; Jeong, M.; Lee, J.; Kim, S.; Yun, H.; Rho, J. Planar Optical Cavities Hybridized with Low-Dimensional Light-Emitting Materials. *Adv. Mater.* **2023**, *35* (4), No. e2203889.
(51) Huang, L.; Wang, Y.; Su, H.; Hu, G.; Deng, C.; Sun, Y.; Yun, B.; Zhang, R.; Chen, Y.; Wang, F.; Cui, Y. Manipulating valley-polarized photoluminescence of $MoS_2$ monolayer at off resonance wavelength with a double-resonance strategy. *Appl. Phys. Lett.* **2021**, *119* (3), No. 031106.
(52) Li, Z.; Liu, C.; Rong, X.; Luo, Y.; Cheng, H.; Zheng, L.; Lin, F.; Shen, B.; Gong, Y.; Zhang, S.; Fang, Z. Tailoring $MoS_2$ Valley-Polarized Photoluminescence with Super Chiral Near-Field. *Adv. Mater.* **2018**, *30*, No. e1801908.
(53) Wen, T.; Zhang, W.; Liu, S.; Hu, A.; Zhao, J.; Ye, Y.; Chen, Y.; Qiu, C. W.; Gong, Q.; Lu, G. Steering valley-polarized emission of monolayer $MoS_2$ sandwiched in plasmonic antennas. *Sci. Adv.* **2020**, *6* (21), No. eaao0019.
(54) Sun, J.; Hu, H.; Pan, D.; Zhang, S.; Xu, H. Selectively Depopulating Valley-Polarized Excitons in Monolayer $MoS_2$ by Local Chirality in Single Plasmonic Nanocavity. *Nano Lett.* **2020**, *20* (7), 4953−4959.
(55) Lin, W. H.; Wu, P. C.; Akbari, H.; Rossman, G. R.; Yeh, N. C.; Atwater, H. A. Electrically Tunable and Dramatically Enhanced Valley-Polarized Emission of Monolayer $WS_2$ at Room Temperature with Plasmonic Archimedes Spiral Nanostructures. *Adv. Mater.* **2022**, *34* (3), No. e2104863.
(56) Chen, Z.; Shen, F.; Zhang, Z.; Wu, K.; Jin, Y.; Long, M.; Wang, S.; Xu, J. Synergistic Effect of Chiral Metasurface and Hot Carrier Injection Enabling Manipulation of Valley Polarization of WSe2 at Room Temperature. *Advanced Physics Research* **2024**, *3*, 2300062.
(57) Yang, L.; Yuan, Y.; Fu, B.; Yang, J.; Dai, D.; Shi, S.; Yan, S.; Zhu, R.; Han, X.; Li, H.; Zuo, Z.; Wang, C.; Huang, Y.; Jin, K.; Gong, Q.; Xu, X. Revealing broken valley symmetry of quantum emitters in $WSe_2$ with chiral nanocavities. *Nat. Commun.* **2023**, *14* (1), 4265.
(58) Wu, Z.; Li, J.; Zhang, X.; Redwing, J. M.; Zheng, Y. Room-Temperature Active Modulation of Valley Dynamics in a Monolayer Semiconductor through Chiral Purcell Effects. *Adv. Mater.* **2019**, *31* (49), No. e1904132.
(59) Landau, L. D.; Lifshitz, E. M. *Electrodynamics of Continuous Media*, 2nd ed.; Pergamon Press: Oxford, U.K., 1984.
(60) Tang, Y.; Cohen, A. E. Optical chirality and its interaction with matter. *Phys. Rev. Lett.* **2010**, *104* (16), 163901.
(61) Schäferling, M.; Dregely, D.; Hentschel, M.; Giessen, H. Tailoring Enhanced Optical Chirality: Design Principles for Chiral Plasmonic Nanostructures. *Physical Review X* **2012**, *2* (3), No. 031010.


https://doi.org/10.1021/acs.nanolett.5c01583
Nano Lett. XXXX, XXX, XXX−XXX

(62) Kang, D.; Onwukaeme, C.; Park, K.; Jeon, K.; Ryu, H. Y.; Yoo, S. Nanophotonic route to control electron behaviors in 2D materials. *Nanophotonics* **2024**, *13* (16), 2865−2878.
(63) Ren, J.; Franke, S.; VanDrunen, B.; Hughes, S. Classical Purcell factors and spontaneous emission decay rates in a linear gain medium. *Phys. Rev. A* **2024**, *109* (1), No. 013513.
(64) Wu, K.; Zhong, H.; Guo, Q.; Tang, J.; Zhang, J.; Qian, L.; Shi, Z.; Zhang, C.; Yuan, S.; Zhang, S.; Xu, H. Identification of twist-angle-dependent excitons in $WS_2/WSe_2$ heterobilayers. *Natl. Sci. Rev.* **2022**, *9* (6), No. nwab135.
(65) Wang, T.; Miao, S.; Li, Z.; Meng, Y.; Lu, Z.; Lian, Z.; Blei, M.; Taniguchi, T.; Watanabe, K.; Tongay, S.; Smirnov, D.; Shi, S. F. Giant Valley-Zeeman Splitting from Spin-Singlet and Spin-Triplet Interlayer Excitons in $WSe_2/MoSe_2$ Heterostructure. *Nano Lett.* **2020**, *20* (1), 694−700.
(66) Kioseoglou, G.; Hanbicki, A. T.; Currie, M.; Friedman, A. L.; Gunlycke, D.; Jonker, B. T. Valley polarization and intervalley scattering in monolayer $MoS_2$. *Appl. Phys. Lett.* **2012**, *101* (22), 221907.
(67) Gorkunov, M. V.; Antonov, A. A.; Kivshar, Y. S. Metasurfaces with Maximum Chirality Empowered by Bound States in the Continuum. *Phys. Rev. Lett.* **2020**, *125* (9), No. 093903.
(68) Changli, J.; Schwiebert, L. Error masking probability of 1's complement checksums. In *Proceedings Tenth International Conference on Computer Communications and Networks (Cat. No.01EX495)*; Scottsdale, AZ, October 15−17, 2001; IEEE, 2001; pp 505−510. DOI: 10.1109/ICCCN.2001.956312.
(69) Li, C.-Y.; He, J.; Zhou, Y.; Qi, D.-X.; Jing, H.; Su, J.; Peng, R.-W.; Fan, R.-H.; Huo, P.; Xu, T.; Wang, M. Flexible perovskite nanosheet-based photodetectors for ultraviolet communication applications. *Appl. Phys. Lett.* **2021**, *119* (25), 251105.
(70) Blair, C. R. On Computer Transcription of Manual Morse. *Journal of the ACM* **1959**, *6* (3), 429−442.


https://doi.org/10.1021/acs.nanolett.5c01583
*Nano Lett.* XXXX, XXX, XXX−XXX